# A Survey of Nanoindentation Studies on HPT-Processed Materials

*In-Chul Choi and Jae-il Jang**

The development of high-pressure torsion (HPT) processing has increased the possibility for achieving significant grain refinement, which leads to a material's ability to produce ultrafine-grained or nanocrystalline materials having enhanced strength without a large expense of ductility at room temperature. Since the applied strain is locally changed across the sample disc during HPT, the microstructure and thus mechanical properties vary within the disc. Recently, as a promising tool for characterizing the mechanical behavior of the local regions within the disc, the nanoindentation technique becomes widely used mainly due to its simple and easy testing procedures and the requirement of only small volume of material. The nanoindentation technique provides important clues to better understand the relation between microstructural refinement and mechanical property enhancement of the HPT-processed materials. Here, the nanoindentation studies performed on various HPT-processed materials are reviewed with focus on a variety of micromechanical properties that can be estimated by nanoindentation and the interesting results are reported in the available literature.

## 1. Introduction

The grain size, $d$, is one of the most important microstructural scales to determine the mechanical properties of a polycrystalline material. It is well accepted that most materials with smaller $d$ exhibit superior strength $\sigma$ for either yielding ($\sigma_y$) or plastic flow ($\sigma_f$), generally in a way of so-called Hall–Petch relation[1,2]

$$\sigma = \sigma_0 + k_{H-P} d^{-0.5} \tag{1}$$

where $\sigma_0$ is the friction stress that is free from grain boundary (GB) contributions, and $k_{H-P}$ is a material constant that is often referred to as the locking parameter or Hall–Petch coefficient. Following this relation, ultrafine-grained (ufg) materials (having $d$ in the range of 0.1–1 μm) and nanocrystalline (nc)

materials (with $d \leq 100$ nm) are known to show significantly enhanced strength.[3] In addition, compared with conventional coarse-grained (cg) counterparts, ufg and nc materials are reported to possibly show increased superplastic formability at high temperature and/or high strain.[4,5] Thus, structural materials with smaller $d$ are attractive for various industrial applications.[6,7]

One of the popular ways to produce ufg and nc materials is introducing exceptionally high strain on bulky single-crystal (sx) or cg materials, which is so-called severe plastic deformation (SPD) process.[8–10] The high dislocation density induced by high straining results in microstructural rearrangement and the forming of an array of GBs. Several SPD techniques are now available such as equal-channel angular pressing (ECAP),[11] high-pressure torsion (HPT),[12] accumulative roll-bonding (ARB),[13] multi-directional forging (MDF),[14] and twist extrusion (TE).[15] Among these SPD techniques, the HPT processing leads to exceptional level of grain refinement that is not generally achieved by other procedures.[16–23] The major advantage of the HPT process is that bulk ufg and nc materials can be produced without involving any major changes in the overall dimensions of the workpieces, some degree of residual porosity, and undesirable crack.[3,18,21–24] These HPT-processed ufg and nc materials show a remarkable combination of superior strength and good ductility which results from significant increase in the fraction of high-angle GBs.[3,4,7,9,10,17,18,21,22] Such high fraction of GBs can also change the predominant deformation mechanisms in ufg and nc.[24]

The equivalent strain applied to a HPT disc (which has generally a diameter of 10 mm and a thickness of $\approx$0.8 mm) can be calculated as[22,25,26]

$$\varepsilon_{eq} = \frac{1}{\sqrt{3}} \frac{2\pi N r}{t_D} \tag{2}$$

where $r$ is the distance from the disc center, $N$ is the number of revolutions, and the $t_D$ is the thickness of the disc. Since the strain proportionally varies with $r$, the microstructure and thus mechanical properties change within the 10-mm-diameter disc. Such local gradient makes it difficult to evaluate the mechanical properties of the HPT-processed disc by performing standard tension tests which inevitably require a larger volume of testing material. One possible way to overcome this limitation is

Prof. I.-C. Choi
School of Materials Science and Engineering
Kumoh National Institute of Technology
Gumi 39177, Republic of Korea

Prof. J.-i. Jang
Division of Materials Science and Engineering
Hanyang University
Seoul 04763, Republic of Korea
E-mail: jijang@hanyang.ac.kr

The ORCID identification number(s) for the author(s) of this article can be found under https://doi.org/10.1002/adem.201900648.

nanoindentation experiment. Its great success is due in part to the simple and easy testing procedure and the requirement of only small volume of a material. It has been also reported that various mechanical properties beyond hardness and reduced modulus can be extracted only from the load ($P$) versus displacement ($h$) curves without additional characterization, which will be introduced below. Furthermore, nanoindentation testing at elevated temperatures is now feasible due to the advances in thermal management techniques.[27] All these advantages make nanoindentation technique a strong tool for estimating the mechanical responses of selected location within the HPT-processed disc,[10] and indeed nanoindentation experiments have continuously played a major role in understanding the deformation mechanisms of HPT-processed materials. Here, nanoindentation studies on various HPT-processed metals and alloys are reviewed with focus on both properties that can be estimated by nanoindentation and the interesting results are reported in the literature.

## 2. Evolution of Hardness during HPT Processing

The fundamental goal of nanoindentation test is to precisely estimate the hardness, $H$, which is also useful for further analysis of time- or temperature-dependent deformation as discussed below. The widely used method to estimate the $H$ value of a material from its $P$–$h$ curve diagram was proposed by Oliver and Pharr.[28,29] The $H$ is determined as

$$H = \frac{P_{max}}{A_c} \tag{3}$$

where $P_{max}$ is the maximum load and $A_c$ is the projected contact area that is a geometrical function of the contact depth, $h_c$. It was reported that even at a given number of revolutions, the equivalent strain of Equation (2) can depend not only on a distance from the disc center but also on that from the disc surfaces.[30] If so, for an accurate interpretation of obtained nanoindentation data, it may be also necessary to define the through-thickness coordinates of the testing position. Nevertheless, in general, this issue is not seriously considered because the ratio of the maximum nanoindentation displacement to the disc thickness ($h_{max}/t_D$) is very small.

**Figure 1** shows nanoindentation results obtained from ufg ZK60 Mg alloy processed by HPT.[31] With increasing $N$, the sizes of the material's bi-modal microstructure are decreased by dynamic recrystallization (DRX) where the concentration of deformation occurs across the new fine grains.[32] In Figure 1, both $H$ values from nanoindentation and Vickers hardness tests show a consistent trend; i.e., $H$ increases rapidly in the early stages of HPT process and thereafter saturates toward the maximum values due to abundant GB strengthening. The higher values were recorded for nanoindentation $H$ compared with Vickers $H$ due to the indentation size effect (ISE), i.e., the $H$ value increases significantly with decreasing $h$ at very shallow depths for nanoindentation with a geometrically self-similar sharp indenter.[33–35]

From nanoindentation tests, it is also possible to estimate the $k_{H−P}$ of Equation (1) based on $H$ data with different $d$ induced by HPT processing. For example, it was reported for face-centered

**In-Chul Choi** is an assistant professor in the School of Materials Science and Engineering at the Kumoh National Institute of Technology in the Republic of Korea. He obtained his B.S. and Ph.D. degrees from the Division of Materials Science and Engineering at Hanyang University in Republic of Korea in 2010 and 2015, respectively, and continued his postdoctoral research at Karlsruhe Institute of Technology in Germany as an Alexander von Humboldt fellow. His research was focused on the small-scale mechanical behavior of advanced metals such as ufg metals, nc/nanotwinned metals, HEAs, and bulk metallic glasses.

**Jae-il Jang** is a professor in the Division of Materials Science and Engineering at Hanyang University in the Republic of Korea. He received his B.S., M.S., and Ph.D. degrees in Metallurgical Science and Engineering from Seoul National University in the Republic of Korea, and worked at the University of Tennessee and Oak Ridge National Laboratory, TN, USA as a postdoctoral fellow and then a research assistant professor. His research focuses on the multiscale mechanical behavior of advanced materials.

cubic (fcc) structured CoCrFeMnNi high-entropy alloy (HEA) processed by HPT.[36] As shown in **Figure 2**, it is apparent that higher $H$ values were recorded for smaller $d$, which is exactly following Hall–Petch relationship. The estimated value of $k_{H−P}$ for the HEA, $\approx 27.7\,MPa(mm)^{1/2}$, is higher than for
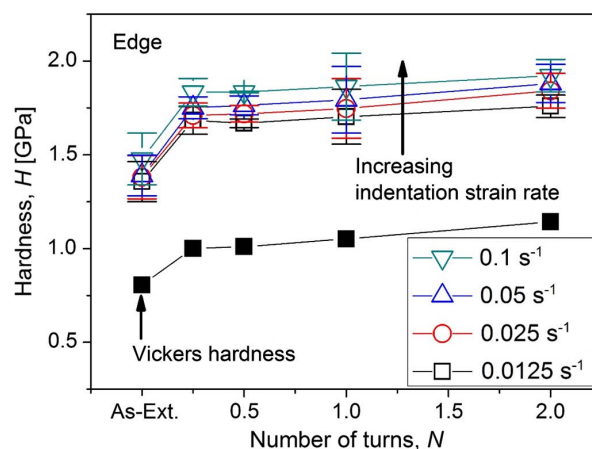


**Figure 1.** Variation in $H$ of ZK60 Mg alloy as a function of $N$ which is compared with Vickers microhardness. Reproduced with permission.[31] Copyright 2014, Elsevier Ltd.
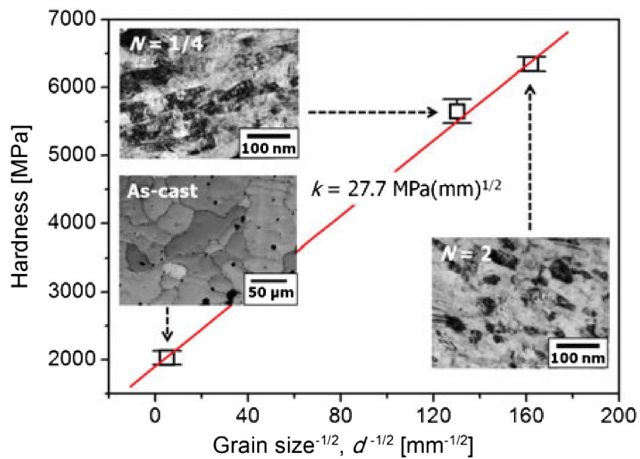
**Figure 2.** Change in $H$ as a function of $d$ in the CoCrFeMnNi HEA system. Reproduced with permission.[36] Copyright 2015, Materials Research Society.

conventional fcc metals where the upper bound value of $k_{H-P}$ is $\approx 19.0$ MPa(mm)$^{1/2}$.[36] This means that the HPT-induced significant hardening in the HEA is mainly due to grain refinement rather than by any other strengthening mechanism including dislocation strengthening.

On the contrary, some ufg materials were reported to exhibit the opposite behavior to Hall–Petch relation; i.e., softening behavior with reducing $d$. An example is the HPT-processed Zn–22%Al eutectoid alloy which consists of a binary microstructure with an Al-rich phase and a Zn-rich phase.[37,38] Although the edge region (i.e., highest strain region) of the HPT-processed disc shows a significant grain refinement to $\approx 350$ nm, the measured nanoindentation $H$ decreases with increasing $N$ at any given indentation strain rate, as shown in **Figure 3**. The reason for the softening can be roughly categorized into two group.[39–42] First, the strain weakening behavior observed in the alloys having low melting temperatures (such as Zn-22%Al alloy[40] and the Pb-62%Sn alloy[41]) generally results from a significant reduction in
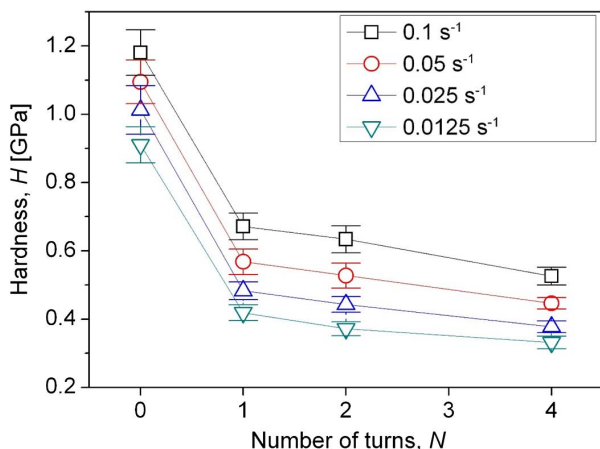
the hard precipitates under severe straining by HPT.[39] Another case of softening behavior was reported for high-purity metals where strain hardening occurs in the very early stage of deformation and then softening follows. This softening is possibly due to the easy cross-slip and microstructural recovery.[42]

## 3. Elastic-to-Elastoplastic Transition Behavior

Nanoindentation testing with a spherical (or blunt) indenter tip makes it possible to estimate the critical shear stress for the incipient plasticity (i.e., yielding or elastic-to-elastoplastic transition) of HPT-processed materials.[31,43,44] The inset graph of **Figure 4** shows an representative example of a $P$–$h$ curve recorded during spherical indentation of a HPT-processed ufg ZK60 Mg alloy. At relatively low $P$, the loading part of the curve (blue-colored, open circle) is completely reversed upon unloading, indicating that the deformation is perfectly elastic. Each curve exhibits so-called "pop-in" that is sudden displacement excursion from the elastic $P$–$h$ curve following Hertzian contact theory[45]
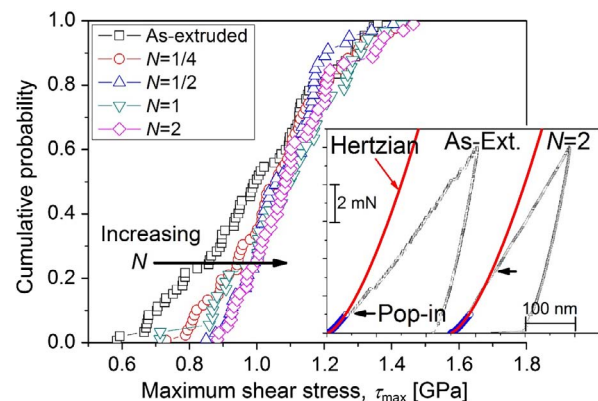
$$P = \frac{4}{3} E_r \sqrt{R} \times h^{\frac{3}{2}} \tag{4}$$

where $R$ is the spherical indenter radius and $E_r$ is the reduced modulus that accounts for the fact that elastic deformation occurs in both the indenter and the sample.[28,29] The value of $R$ can be verified by using Equation (4) after performing indentations on a sample with a known $E_r$ (such as fused silica or tungsten).

The maximum shear stress at the first-pop-in, $\tau_{max}$, represents the critical shear strength for the onset of plasticity in the indented material. Since the pop-in occurs at the elastic curve following elastic contact theory, the magnitude of the $\tau_{max}$ can be easily calculated as[45]

$$\tau_{max} = 0.31 \left( \frac{6 E_r^2}{\pi^3 R^2} P \right)^{\frac{1}{3}} \tag{5}$$

The estimated values of $\tau_{max}$ in the literature are often in the same order as the theoretical shear strength of a defect-free material.[45,46] The HPT-processed ZK60 Mg alloy shows that the



**Figure 3.** Hardness variation of HPT-processed Zn-22%Al alloy with increasing $N$. Reproduced with permission.[37] Copyright 2013, Elsevier Ltd.



**Figure 4.** Cumulative probability distribution of the maximum shear strength ($\tau_{max}$) of HPT-processed ufg ZK60 Mg alloy with increasing $N$ (with the inset image showing representative $P$–$h$ curves with pop-ins). Reproduced with permission.[31] Copyright 2014, Elsevier Ltd.

**ADVANCED
SCIENCE NEWS**

www.advancedsciencenews.com

**ADVANCED
ENGINEERING
MATERIALS**

www.aem-journal.com

average $\tau_{max}$ increases to a saturation level of almost $\approx G/15$ where $G$ is its shear modulus.[31]

Since these $\tau_{max}$ values generally exhibit wide fluctuations due to the complex inhomogeneities in a material, statistical analysis of the pop-in data may be essential to shed light on underlying yielding mechanisms.[44,47] On this basis, the cumulative distribution function of pop-in events can be described as a function of the shear stress beneath the indenter, $\tau$:[47,48]

$$f = 1 - \exp\left[-\frac{kT\dot{\gamma}_0}{V_y^*(d\tau/dt)} \times \exp\left(-\frac{\Delta F^*}{kT}\right) \times \exp\left(\frac{\tau V_y^*}{kT}\right)\right] \quad (6)$$

where $k$ is the Boltzmann constant, $T$ is the absolute temperature, $\dot{\gamma}_0$ is the attempt frequency (that is the frequency of the fundamental mode vibration along the reaction pathway), $\Delta F^*$ and $V_y^*$ are the Helmholtz activation energy and volume of the pop-in event, respectively. Then, at $\tau = \tau_{max}$, $V_y^*$ can be estimated from the slope of $\ln[\ln(1-f)^{-1}]$ versus $\tau_{max}$ plot, which provides the crucial information about the thermally assisted, stress-biased yielding mechanisms. According to the cumulative distribution of $\tau_{max}$ for the HPT-processed ufg ZK60 alloy in Figure 4, all samples exhibit $V_y^* \approx 1b^3$ which corresponds to the yielding by heterogeneous dislocation nucleation.[31,44,48] The measured $V_y^*$ remains constant with increasing $N$, demonstrating that the inherent mechanisms of yielding remain unchanged by HPT.[31] This phenomenon is reasonable because the sizes of the highly stressed zones beneath the spherical indenter are smaller than the averaged $d$ in the HPT-processed discs.

## 4. Stress–Strain Response for Plastic Flow

For practical applications of ufg and nc materials developed with the aid of HPT, it is essential to capture the variation in constitutive stress–strain behavior with $d$ within the HPT-processed discs. In this regard, a promising way to estimate stress–strain behavior (especially for a relatively large plastic regime) can be nanoindentation tests with several triangular pyramidal indenters having different values of "sharpness" that can be identified by centerline-to-face angle, $\psi$. Since a sharper indenter induces a larger strain in the material, indentations made with different $\psi$ allow a systematic evaluation of the stress–strain response and work-hardening exponent. An example is shown in **Figure 5**a that provides representative $P$–$h$ curves of the HPT-processed CoCrFeMnNi HEA without and with annealing treatment at 723 K for 1 h (HPT + 1A) and 10 h (HPT + 10A). The $H$ value obtained from the curve can be converted into $\sigma_f$ by using the Tabor's well-known empirical relationship[49]

$$H = C_\theta \times \sigma_f \quad (7)$$

where $C_\theta$ is the constraint factor and $\theta$ is the half-angle of a "conical" indenter. The value of $C_\theta$ is typically in the range of $\approx 2.6$–$3.0$ for metallic materials in the fully plastic regime of indentations but also depends on both $\theta$ and the level of plasticity attained underneath the indenter. By assuming that identical indentation responses are obtained when $h$ gives the same area-to-depth ratio as the pyramid, the relation between $\psi$ and $\theta$ is given as[50–52]
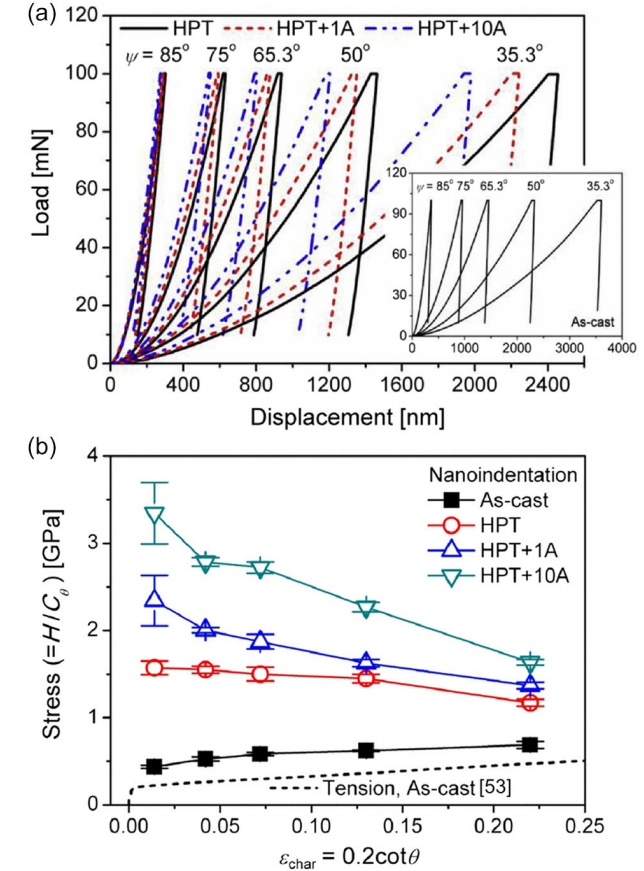


**Figure 5.** a) Typical $P$–$h$ curves of the HPT-processed CoCrFeMnNi samples without and with annealing treatment at 723 K for 1 h (HPT + 1A) and 10 h (HPTt + 10A), which are obtained from nanoindenetation testing with sharp indenter tips having five different $\psi$ (with the inset image showing the curves for as-cast sample). b) The variations in $\sigma_f$ with $\varepsilon_{char}$ for as-cast CoCrFeMnNi HEA and HPT-processed nc CoCrFeMnNi HEA with or without isochronal annealing. The tensile test data for the as-cast HEA[53] is also shown for comparison purposes. Reproduced with permission.[52] Copyright 2017, Elsevier Ltd.

$$\theta = \tan^{-1}\left(\sqrt{\frac{3\sqrt{3}}{\pi}}\tan\psi\right) \quad (8)$$

Following Equation (8), e.g., a $\psi$ of 65.3° for Berkovich indenter corresponds to a $\theta$ of 70.3°. The characteristic strain ($\varepsilon_{char}$) for each sharp indenter geometry is defined as[45]

$$\varepsilon_{char} = 0.2 \times \cot\theta \quad (9)$$

By applying Equation (7–9), the plastic flow behavior of the indented samples can be simply estimated as shown in Figure 5b.[52] Although there is a slight difference in stress possibly due to the ISE,[34] the estimated stress–strain response of cg (as-cast) HEA sample is in reasonably good agreement with the result from tensile testing.[52,53] It is interesting to find that all HPT-processed nc HEA samples exhibit strain-softening behavior which is opposite to the work hardening of the cg sample. Strain-softening phenomena have been frequently

**ADVANCED
SCIENCE NEWS**

www.advancedsciencenews.com

**ADVANCED
ENGINEERING
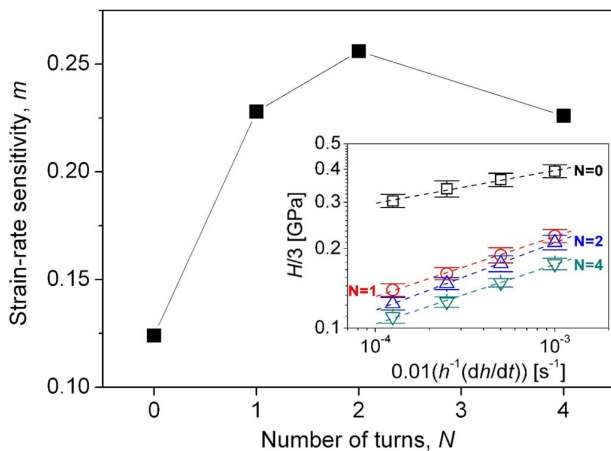MATERIALS**

www.aem-journal.com

observed in tensile and compressive tests of nc and ufg materials because of a variety of possible mechanisms such as extensive dynamic recovery, DRX, and the existence of residual internal stress in GBs.[52] An important feature in Figure 5b is an increase in the amount of the softening with the annealing time, which indicates that additionally possible mechanisms may be at work in the strain softening of the annealed HPT samples. For the additional strain softening, the deformation-assisted dissolution of the precipitates can be one of the reasons, which is rationalized in consideration of the increase in interface energy.[52] In addition, there can be substantial atomic diffusion through the high fraction of GBs in the annealed nc HEA.

## 5. Rate-Dependent Plasticity

The enhancement in ductility can be introduced in ufg and nc metals by the sustained plasticity through activating grain-boundary sliding (GBS), GB-mediated mechanism, and diffusion. In this regard, numerous nanoindentation studies have been performed to demonstrate the rate-dependent plasticity of various HPT-processed materials. Two important indicators for the rate-dependent plastic deformation, i.e., the strain-rate sensitivity ($m$) and activation volume ($V^*$), can be estimated by nanoindentation tests in two different methods: multiple constant strain-rate (CSR) tests and single strain-rate jump (SRJ) tests. According to phenomenologically modelled power–law response between $H$ and indentation strain rate, $\dot{\varepsilon}_i$,[50] the $m$ value can be determined at a given $\varepsilon$ and $T$ by[31,51,54]

$$m = \left(\frac{\partial \ln \sigma_f}{\partial \ln \dot{\varepsilon}}\right)_{\varepsilon,T} = \left(\frac{\partial \ln(H/C_\theta)}{\partial \ln(0.01\dot{\varepsilon}_i)}\right)_{\varepsilon,T} \tag{10}$$

Note that strain rate $\dot{\varepsilon}$ and the indentation strain rate $\dot{\varepsilon}_i$ are related through the empirical relation $\dot{\varepsilon} \approx 0.01\dot{\varepsilon}_i$.[50] Thus, the variation in $m$ can be estimated from slopes of the double logarithmic plots of $H/C_\theta$ versus $\dot{\varepsilon}_i$, as displayed in an inset image of **Figure 6**.[37] The second important parameter for the rate-

dependent deformation is the apparent activation volume for plastic deformation, $V^*$[31,37,51,54–56]

$$V^* = \sqrt{3}kT\left(\frac{\partial \ln \dot{\varepsilon}}{\partial \sigma}\right) \approx \sqrt{3}kT\left(\frac{\partial \ln \dot{\varepsilon}_i}{\partial (H/C_\theta)}\right) \tag{11}$$

These rate-sensitive parameters must be carefully interpreted to determine the thermally activated deformation mechanism because the $m$ and $V^*$ values can vary with applied strain rate, induced strain, temperature, and microstructure.

As listed in **Table 1** that summarizes the $m$ value obtained from HPT-processed materials, grain refinements in fcc materials (such as pure Al,[57] pure Au,[58,59] CoCrFeMnNi HEA,[36,60–62] and $(CoCrFeNi)_{94}Ti_2Al_4$ HEA[63]), hexagonal close-packed (hcp) materials including ZK60 Mg alloy[31], and micro-duplex alloys
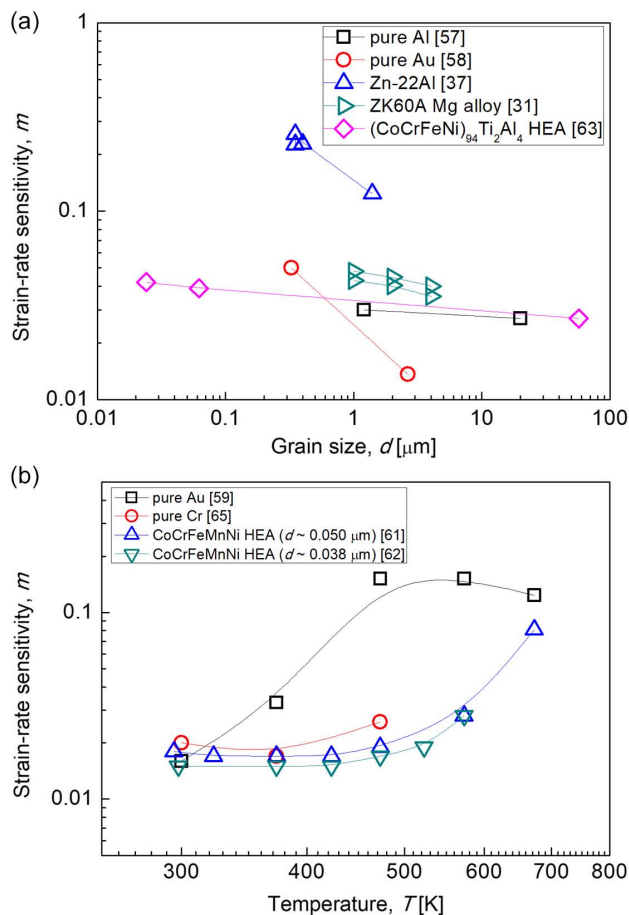
**Table 1.** Summary of strain-rate sensitivity ($m$) values for HPT-processed ufg and nc materials, which were estimated from nanoindentation tests at various temperatures.

| Materials | Grain size, $d$ [μm] | Temperature, $T$ [°C] | Strain-rate sensitivity, $m$ | Ref. |
|---|---|---|---|---|
| Pure Al | 1.2 | RT | 0.030 | [57] |
| Pure Au | 0.325 | RT | 0.050 | [58] |
| | 0.291 | RT | 0.016 | [59] |
| | | 100 | 0.033 | |
| | | 200 | 0.152 | |
| | | 300 | 0.152 | |
| | | 400 | 0.124 | |
| Pure Cr | 0.300 | RT | 0.020 | [65] |
| | | 100 | 0.017 | |
| | | 200 | 0.026 | |
| Al-30%Zn | 0.380 | RT | 0.220 | [57] |
| Zn-22%Al | 0.350 | RT | 0.226–0.256 | [37] |
| Al-Mg | 0.190 | RT | <0.01 | [64] |
| ZK60 Mg alloy | 20 & 2–3 | RT | 0.048 | [31] |
| CoCrFeMnNi HEA | 0.059 | RT | 0.031 | [36] |
| | 0.038 | RT | 0.025 | |
| | 0.050 | RT | 0.018 | [60,61] |
| | | 50 | 0.017 | |
| | | 100 | 0.017 | |
| | | 150 | 0.017 | |
| | | 200 | 0.019 | |
| | | 300 | 0.028 | |
| | | 400 | 0.081 | |
| | 0.038 | RT | 0.015 | [62] |
| | | 100 | 0.015 | |
| | | 150 | 0.015 | |
| | | 200 | 0.017 | |
| | | 250 | 0.019 | |
| | | 300 | 0.028 | |
| $(CoCrFeNi)_{94}Ti_2Al_4$ HEA | 0.062 | RT | 0.039 | [63] |
| | 0.024 | RT | 0.042 | |



**Figure 6.** Variation in strain-rate sensitivity ($m$) of Zn-22%Al alloy with increasing the total number of torsional revolution $N$. The inset image is the double logarithmic plots of $H/C_\theta$ versus $\dot{\varepsilon}_i$. Reproduced with permission.[37] Copyright 2013, Elsevier Ltd.

**ADVANCED
SCIENCE NEWS**
www.advancedsciencenews.com

**ADVANCED
ENGINEERING
MATERIALS**
www.aem-journal.com

(such as Zn-Al alloy[37,57] and Al-Mg alloy[64]) generally lead to an enhanced $m$ value in comparison with that of cg materials.[31,37,57,58,63] This trend is clearly seen in **Figure 7**a, where the $m$ values are given as a function of $d$. Figure 7b exhibits the change in $m$ with testing temperature. As one can expect, the $m$ value increases with the temperature.

Especially, as shown in Figure 3 and 6, the Zn-Al alloy[37] with relatively high ductility and low melting point shows a significant rate-dependency on the $H$ value which becomes more pronounced after HPT; i.e., the $m$ value of the as-annealed sample increases dramatically up to $\approx 0.26$ after the HPT process. Through analysis of the nanoindentation impressions (**Figure 8**), these enhanced $m$ values are affected by the shear-off behavior by GBS which is apparent in the pile-up region due to the different microstructural size.[37] However, the calculated values of $V^*$ are almost constant as $\approx 8.5$–$11.4b^3$ which suggests GBS as the predominant deformation mechanism for both the unprocessed and HPT-processed samples.

In contrast to fcc- or hcp-structured materials, the $m$ value of body-centered cubic (bcc) structured Cr has an opposite dependency on grain refinement. Upon HPT processing for producing ufg Cr, the $m$ value is significantly decreased compared with the sx counterpart ($m \approx 0.07$).[65] The pronounced rate-sensitive deformation behavior in bcc metals is closely related to the
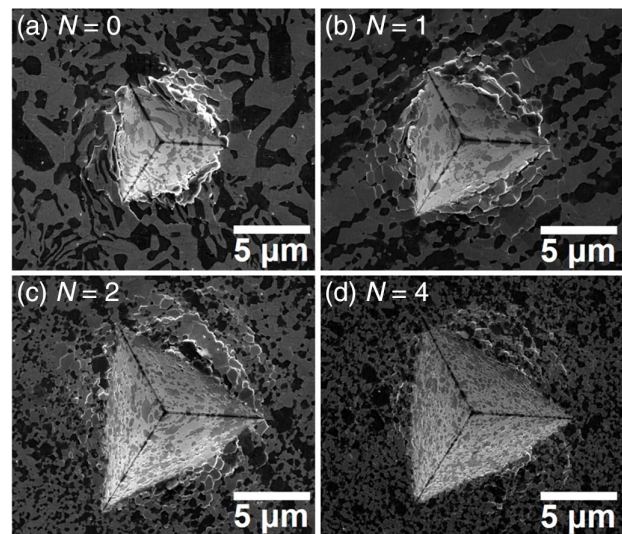


**Figure 8.** SEM images on morphology around impressions after nanoindentation experiments a) as-annealed Zn-22%Al sample without HPT and the alloy with HPT straining for b) 1 turn, c), 2 turns, and d) 4 turns. Reproduced with permission.[37] Copyright 2013, Elsevier Ltd.

athermal stress which affect a limited mobility of screw dislocations due to their non-planar dislocation core structure.[65,66] The reduced $m$ value of bcc metals is caused by the strongly enhanced athermal stress component due to the increase in volume fraction of GBs by HPT processing.

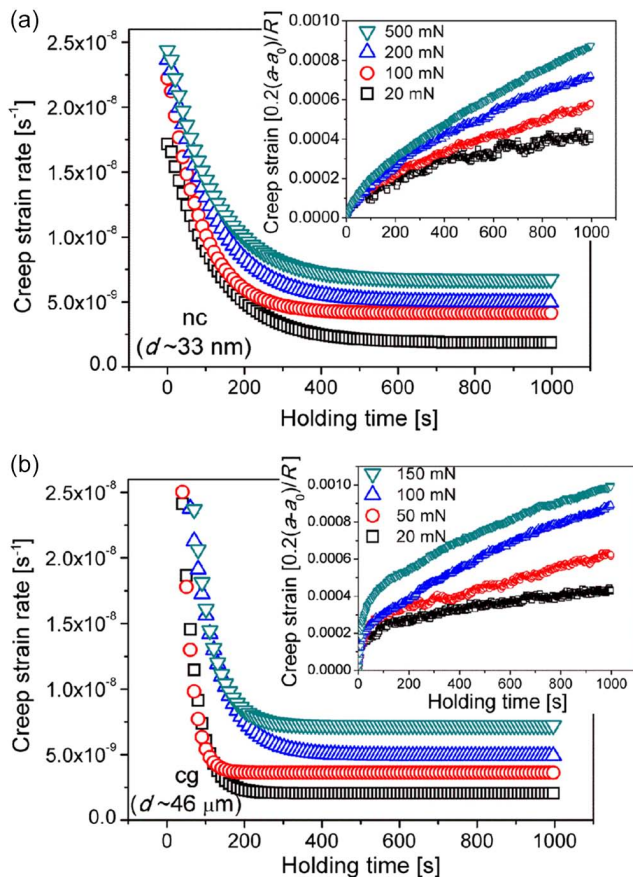## 6. Room-Temperature Nanoindentation Creep Behavior

In the HPT-processed ufg and nc materials, the large fraction of GBs is considered to be in a non-equilibrium state due to their excess extrinsic dislocations, higher energy, and larger free volume or vacancy concentration than in common GBs in cg materials.[67] Therefore, it is possible that HPT-processed materials exhibit diffusion-related deformation processes such as creep even at relatively low temperatures such as room temperature (RT). Usually, the constant-load nanoindentation test is widely used for evaluating the creep deformation because of its close resemblance of load scheme (load-hold at peak load) to that in the conventional uniaxial creep test; the sample is quasi-statically loaded to a predetermined peak load, then the load is held constant, and the increase in $h$ with holding time, $t$, is monitored. From the $h$ versus $t$ data, the change in $\sigma_f$ with $t$ can be estimated. To estimate the displacement rate ($dh/dt$), which is required for computing the indentation strain rate for the creep regime, $\dot{\varepsilon}_i = (dh/dt)/h$, the $h$–$t$ data is fitted with an empirical equation[68,69]
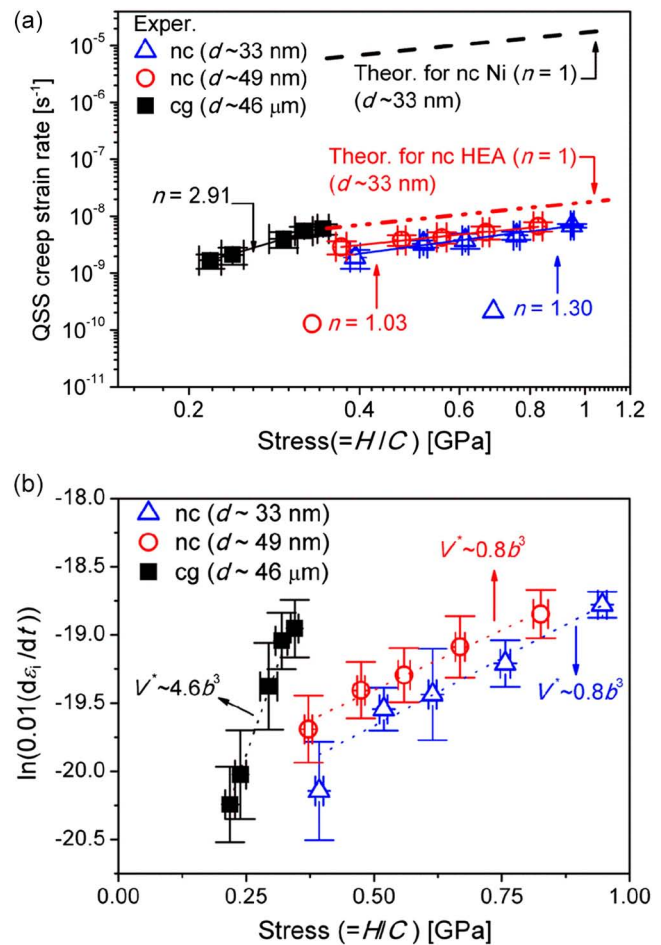
$$h(t) = h_0 + At^\kappa + Bt \tag{12}$$

where $h_0$ is the indentation depth at load-hold at peak load, and $A$, $B$, and $\kappa$ are fitting constants. In creep test, the steady-state creep strain rate, $\dot{\varepsilon}_{ss}$, is sensitive to the applied stress, $\sigma$, and varies according to $\dot{\varepsilon}_{ss} \propto \sigma^n$, where $n$ is the creep stress exponent.



**Figure 7.** Variation in the strain-rate sensitivity ($m$) of various materials with a) grain size and b) testing temperature.

Thus, the $n$ value can be obtained by plotting $\sigma$ versus $\dot{\varepsilon}_{ss}$ on a log–log scale.

In many studies, the indentation creep behavior has been analyzed through the tests with a "sharp" tip.[41,59] However, these results have to be analyzed carefully because there are some critical issues related to the sharp tip geometry. Detailed explanations for the issues are introduced elsewhere.[54] To solve the issues related to sharp tip geometry, nanoindentaion creep tests with a "spherical" tip were performed on the HPT-processed CoCrFeMnNi HEA.[67] In spherical indentation, both the $\varepsilon_{char}$ and the $\sigma_f$ (i.e., $H$) at the onset of creep can be changed by varying the applied $P_{max}$. As shown in **Figure 9**, creep deformation indeed occurs in both cg and nc HEAs even at RT, and it is more pronounced with increasing $P_{max}$. From the variations in $\dot{\varepsilon}_{ss}$ with $\sigma_f$ for nc and cg HEAs summarized in **Figure 10**a, $n$ was determined as $\approx 1$ for the nc HEAs and $\approx 3$ for the cg HEA. This implies that the creep is mainly governed by diffusion-related mechanism in nc HEAs while the creep deformation of the cg HEA is primarily controlled by dislocation-mediated mechanism. Moreover, further insight into the creep mechanism can be obtained by calculating the value of $V^*$ according to Equation (11). For instance, the $V^*$ for nc HEAs is smaller than $V^*$ of cg HEA as shown in Figure 10b. Since the influence of GB

**Figure 10.** a) Double logarithmic plot between quasi-steady state (QSS) creep strain rate and stress where the slope corresponds to the creep stress exponent, $n$, and b) logarithmic strain rate versus linear stress relation to estimate the activation volume $V^*$ for creep. Reproduced with permission.[67] Copyright 2016, Elsevier Ltd.

**Figure 9.** Strain rate versus holding time (with the inset showing creep strain versus holding time). a) nc HEA for $d \approx 33$ nm and b) cg HEA for $d \approx 46$ µm. Reproduced with permission.[67] Copyright 2016, Elsevier Ltd.

diffusion on $\dot{\varepsilon}_{ss}$ of nc HEAs is significantly larger than that of lattice diffusion, creep deformation of nc materials is mainly governed by GB diffusion and its related deformation mechanisms such as Coble creep, GB sliding, GB migration, and GB rotation. In addition, through comparison of a theoretical creep rate between fcc-structured nc HEA and conventional nc metal having fcc structure (i.e., Ni), it was revealed that the creep resistance of nc HEA is significantly enhanced by sluggish diffusion which is distinct characteristics of HEAs.

## 7. Apparent Activation Energy

Since all mechanical properties characterized by nanoindentation can strongly depend on testing temperature (Figure 7b), nanoindentation tests at various temperatures can provide some important information for high-temperature (HT) applications of structural materials.[27,59,61,62] Keeping this in view, several HT nanoindentation experiments have been performed on the HPT-processed ufg and nc materials.[58,59,61,62] In the early

**ADVANCED
SCIENCE NEWS**

www.advancedsciencenews.com

**ADVANCED
ENGINEERING
MATERIALS**

www.aem-journal.com

HT nanoindentation studies on HPT-processed materials, most research was focused on the temperature dependency on various mechanical properties, such as $H$, $m$, $n$, and $V^*$. Above all things, the HT nanoindentation makes it feasible to completely understand a material's thermally activated plastic deformation process through estimating the apparent activation energy, $Q$. The Boltzmann-type constitutive law for temperature-dependent plastic strain rate is given as

$$\dot{\varepsilon} = \dot{\varepsilon}_0 \exp(-Q/kT) \approx \dot{\varepsilon}_0 \exp(-\Delta\mathcal{H}/kT) \qquad (13)$$

where $\dot{\varepsilon}_0$ is a pre-exponential constant and the $Q$ is described as the stress-dependent Gibbs free energy $\Delta G$ for the activation of flow. Since the entropy for plastic flow tends to be very small, $\Delta G$ is often assumed to be equal to the apparent activation enthalpy, $\Delta\mathcal{H}$.[70] Then, $\Delta\mathcal{H}$ can be determined as[62,71]

$$\Delta\mathcal{H} = -kT^2 \frac{\partial \ln(\dot{\varepsilon}/\dot{\varepsilon}_0)}{\partial T} \approx -kT^2 \frac{\partial \ln \dot{\varepsilon}_i}{\partial H} \times \frac{\partial H}{\partial T}$$
$$= -T \frac{V^*}{\sqrt{3}C_\theta} \left(\frac{\partial H}{\partial T}\right) = \frac{HV^*}{\sqrt{3}C_\theta T} \times \frac{\partial \ln H}{\partial(1/T)} \qquad (14)$$

Typically, a relatively low $\Delta\mathcal{H}$ estimated by using Equation (14) suggests that deformation is governed by GB-mediated dislocation activities such as the emission of partial or perfect dislocations from GBs, for which the activation barrier is expected as 0.7–1 eV.[62,71] The relatively high $\Delta\mathcal{H}$ ($\approx$2 eV) approaches that for GB diffusion mechanisms, which can be related with a large volume of non-equilibrium GBs in HPT-processed nc materials.[72]

**Figure 11**a shows the variations in $H$ with $1/T$ of cg and nc CoCrFeMnNi HEAs. Due to the grain refinement, the $H$ value of nc HEA is much higher than that of cg HEA at a given temperature.[62] In contrast to cg HEA's response within the whole temperature range, nc HEA shows a bilinear response in $\ln(H)$ versus $1/T$ plot with a considerable change in the slope at $\approx$473 K. Although the sudden changes in the $m$ value also observed from 473 K onward with $T$ (Table 1), these variations are not sufficient to confirm a mechanistic transition, which indicate a possible change in the deformation mechanism.[61,62] A transition in the thermally activated deformation mechanism of nc HEA is described by estimating the $\Delta\mathcal{H}$ from the change in slope observed in Figure 11a. As shown in Figure 11b, the estimated $\Delta\mathcal{H}$ for $T \leq 473$ K ($\approx$0.3$T_m$) is relatively low which suggests that deformation is governed by GB-mediated dislocation activities such as the emission of partial or perfect dislocations from GBs.[71] Then, for $T > 473$ K ($\approx$0.3$T_m$), there is a marked and sharp increase in $\Delta\mathcal{H}$. This relatively high value approaches that for GB diffusion of Ni in CoCrFeMnNi HEA,[73] which may be closely related to a large volume of non-equilibrium GBs in HPT-processed nc HEA.[62,72]

## 8. Conclusions

To enhance the mechanical properties through grain refinement from sx or cg to ufg or nc, various SPD processes have been popularly performed. Compared with other SPD techniques, the HPT processing leads to exceptional grain refinement in a
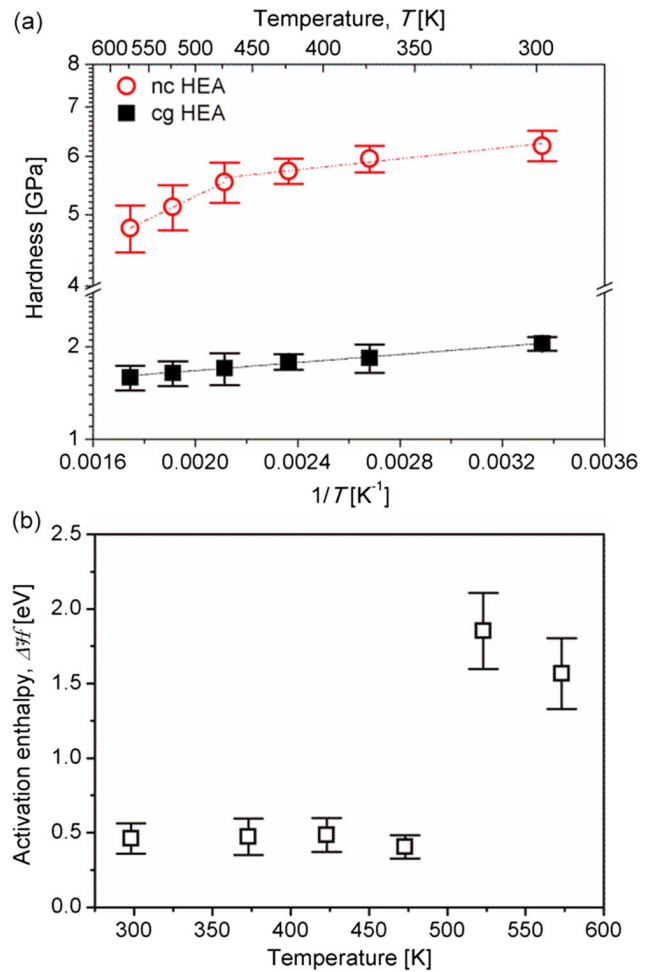


**Figure 11.** Results of the HT nanoindentation experiments on HPT-processed nc CoCrFeMnNi HEA: a) the variation in $H$ as a function of $1/T$ of nc and cg HEA; b) the variations of the apparent activation enthalpy, $\Delta\mathcal{H}$, of nc HEA with $T$. Reproduced with permission.[62] Copyright 2018, Elsevier Ltd.

material due to very high straining. For better understanding of the relation between refined microstructure and mechanical behavior of HPT-processed materials, the nanoindentation technique has been widely used under various rate and temperature conditions, which makes it possible to estimate various mechanical properties of the local regions within a HPT disc. This review focused upon the results of nanoindentation study for HPT-processed materials with the following aspects: 1) Due to a GB strengthening induced by HPT processing, the measured $H$ values of most materials increase with increasing $N$. However, some commercial metals and alloys show the strain weakening that results from either a significant reduction in the hard precipitates or the microstructural recovery under severe straining by HPT. 2) Nanoindentation testing with a spherical tip makes it possible to examine elastic-to-elastoplastic transition behavior of HPT-processed materials, which is observed as pop-in(s) during loading sequence. The statistical analysis of the pop-in data may shed light on underlying inherent mechanisms for the incipient plasticity of the HPT-processed materials. 3) Through

nanoindentation tests with a variety of sharp tips having different sharpness, it is possible to show the constitutive stress–strain behavior for the large plastic regime of HPT-processed materials. 4) To investigate the rate-dependent plastic deformation which is related with enhancement in ductility of ufg and nc materials processed by HPT, the $m$ and $V^*$ values can be estimated by using nanoindentation tests. The obtained $m$ and $V^*$ is feasible for better understanding of thermally activated plastic deformation including superplasticity of HPT-processed materials. 5) Since ufg and nc materials processed by HPT include the substantial fraction of GBs, diffusion-related deformation, such as creep, can occur even at RTs. A nanoindentation test with a spherical tip can provide the useful parameters for showing creep mechanisms. 6) To examine material's behavior at the industrial service conditions, HT nanoindentation experiments have been also performed on the HPT-processed materials. Through the tests, it is feasible not only to measure temperature-dependent $H$ data but also to completely understand a material's thermally activated plastic deformation process through estimating activation energy.

## Conflict of Interest

The authors declare no conflict of interest.

[1] E. O. Hall, *Proc. Phys. Soc. London, Sect. B* **1951**, *64*, 747.

[2] N. J. Petch, *J. Iron. Steel. Inst.* **1953**, *174*, 25.

[3] R. Z. Valiev, Y. Estrin, Z. Horita, T. G. Langdon, M. J. Zehetbauer, Y. T. Zhu, *JOM* **2006**, *58*(4), 33.

[4] M. Kawasaki, T. G. Langdon, *J. Mater. Sci.* **2016**, *51*, 19.

[5] M. Dao, L. Lu, Y. F. Shen, S. Suresh. *Acta Mater.* **2006**, *54*, 5421.

[6] T. C. Lowe, *JOM* **2006**, *58*, 28.

[7] R. Z. Valiev, I. Sabirov, A. P. Zhilyaev, T. G. Langdon, *JOM* **2012**, *64*, 1134.

[8] Y. T. Zhu, T. C. Lowe, T. G. Langdon, *Scripta Mater.* **2004**, *51*, 825.

[9] T. G. Langdon, *J. Mater. Sci.* **2007**, *42*, 3388.

[10] M. Kawasaki, B. Ahn, P. Kumar, J.-i. Jang, T. G. Landon, *Adv. Eng. Mater.* **2017**, *19*, 1600578.

[11] V. M. Segal, V. I. Reznikov, A. E. Drobyshevskiy, V. I. Kopylov, *Russ. Metall.* **1981**, *1*, 99.

[12] N. A. Smirnova, V. I. Levit, V. I. Pilyugin, R. I. Kuznetsov, L. S. Davydova, V. A. Sazonova, *Fiz. Metal. Metalloved* **1986**, *61*, 1170.

[13] Y. Saito, N. Tsuji, H. Utsunomiya, T. Sakai, R. G. Hong, *Scripta Mater.* **1998**, *39*, 1221.

[14] G. A. Salishchev, O. R. Valiahmetov, R. M. Galeev, *J. Mater. Sci.* **1993**, *28*, 2898.

[15] V. N. Varyutkhin, Y. Y. Beygelzimer, S. Synkov, D. Orlov, *Mater. Sci. Forum* **2006**, *503–504*, 33.

[16] G. Sakai, K. Nakamura, Z. Horita, T. G. Langdon, *Mater. Sci. Eng. A* **2005**, *406*, 268.

[17] Y. Estrin, H. J. Maier, *Mater. Sci. Forum* **2008**, *584–586*, 16.

[18] A. P. Zhilyaev, T. G. Langdon, *Prog. Mater.* **2008**, *53*, 893.

[19] A. Hohenwarter, A. Bachmaier, B. Gludovatz, S. Scheriau, R. Pippan, *Int. J. Mater. Res.* **2009**, *100*, 1653.

[20] Y. Harai, K. Edalati, Z. Horita, T. G. Langdon, *Acta Mater.* **2009**, *57*, 1147.

[21] R. Pippan, S. Scheriau, A. Taylor, M. Hafok, A. Hohenwarter, A. Bachmaier, *Ann. Rev. Mater. Res.* **2010**, *40*, 319.

[22] T. G. Langdon, *Acta Mater.* **2013**, *61*, 7035.

[23] K. Edalati, Z. Horita, *Mater. Sci. Eng. A* **2016**, *652*, 325.

[24] R. Valiev, *Nat. Mater.* **2004**, *3*, 511.

[25] R. Z. Valiev, Y. V. Ivanisenko, E. F. Rauch, B. Baudelet, *Acta Mater.* **1996**, *44*, 4705.

[26] F. Wetscher, A. Vorhauer, R. Stock, R. Pippan. *Mater. Sci. Eng. A* **2004**, *387-389*, 809.

[27] J. M. Wheeler, D. E. J. Armstrong, W. Heinz, R. Schwaiger, *Curr. Opin. Solid State Mater. Sci.* **2015**, *19*, 354.

[28] W. C. Oliver, G. M. Pharr, *J. Mater. Res.* **1992**, *7*, 1564.

[29] W. C. Oliver, G. M. Pharr, *J. Mater. Res.* **2002**, *19*, 3.

[30] Y. Beygelzimer, R. Kulagin, L. S. Toth, Y. Ivanisenko, *Beilstein J. Nanotechnol.* **2016**, *7*, 1267.

[31] I.-C. Choi, D.-H. Lee, B. Ahn, K. Durst, M. Kawasaki, L. T. Langdon, J.-i. Jang, *Scripta Mater.* **2015**, *94*, 44.

[32] R. B. Figueiredo, T. G. Langdon, *J. Mater. Sci.* **2010**, *45*, 4827.

[33] G. M. Pharr, E. G. Herber, Y. Gao, *Annu. Rev. Mater. Res.* **2010**, *40*, 271.

[34] W. D. Nix, H. Gao, *J. Mech. Phys. Solids* **1998**, *46*, 411.

[35] I.-C. Choi, Y. Zhao, Y.-J. Kim, B.-G. Yoo, J.-Y. Suh, U. Ramamurty, J.-I. Jang, *Acta Mater.* **2012**, *60*, 6862.

[36] D.-H. Lee, I.-C. Choi, M.-Y. Seok, J. He, Z. Lu, J.-Y. Suh, M. Kawasaki, T. G. Langdon, J.-i. Jang, *J. Mater. Res.* **2015**, *30*, 2804.

[37] I.-C. Choi, Y.-J. Kim, B. Ahn, M. Kawasaki, T. G. Langdon, J.-i. Jang, *Scripta Mater.* **2014**, *75*, 102.

[38] M. Kawasaki, B. Ahn, T. G. Langdon, *Acta Mater.* **2010**, *58*, 919.

[39] M. Furukawa, Z. Horita, M. Nemoto, R. Z. Valiev, T. G. Langdon, *J. Mater. Res.* **1996**, *11*, 2128.

[40] T.-S. Cho, H.-J. Lee, B. Ahn, M. Kawasaki, T. G. Langdon, *Acta Mater.* **2014**, *72*, 67.

[41] N. X. Zhang, N. Q. Chinh, M. Kawasaki, Y. Huang, T. G. Langdon, *Mater. Sci. Eng. A* **2016**, *666*, 350.

[42] C. Xu, Z. Horita, T. G. Langdon, *Acta Mater.* **2007**, *55*, 203.

[43] T. F. Page, W. C. Oliver, C. J. McHargue, *J. Mater. Res.* **1992**, *7*, 450.

[44] C. A. Schuh, J. K. Mason, A. C. Lund, *Nat. Mater.* **2005**, *4*, 617.

[45] K. L. Johnson, *Contact Mechanics*, Cambridge University Press, Cambridge **1985**.

[46] G. E. Dieter, *Mechanical Metallurgy*, McGraw-Hill Book Company, London **1988**.

[47] I.-C. Choi, Y. Zhao, Y.-J. Kim, B.-G. Yoo, J.-Y. Suh, U. Ramamurty, J.-i. Jang, *Acta Mater.* **2012**, *60*, 6868.

[48] C. A. Schuh, A. C. Lund, *J. Mater. Res.* **2004**, *19*, 2152.

[49] D. Tabor, *The Hardness of Metals*, Oxford University Press, Oxford **1951**.

[50] A. C. Fischer-Cripps, *Nanoindentation*, Springer Science+Business Media, New York, USA **2011**.

[51] I.-C. Choi, Y.-J. Kim, Y. M. Wang, U. Ramamurty, J.-i. Jang, *Acta Mater.* **2013**, *61*, 7313.

[52] D.-H. Lee, J.-A Lee, Y. Zhao, Z. Lu, J.-Y. Suh, J.-Y. Kim, U. Ramamurty, M, Kawasaki, T. G. Langdon, J.-i. Jang, *Acta Mater.* **2017**, *140*, 443.

[53] Y. Wu, W. H. Liu, X.L. Wang, D. Ma, A. D. Stoica, T. G. Nieh, Z. B. He, Z. P. Lu, *Appl. Phys. Lett.* **2014**, *104*, 051910.

[54] I.-C. Choi, B.-G. Yoo, Y.-J. Kim, J.-i. Jang, *J. Mater. Res.* **2012**, *27*, 3.

[55] V. Maier, K. Durst, J. Mueller, B. Backes, H.W. Höppel, M. Göken, *J. Mater. Res.* **2011**, *26*, 1421.

[56] D. Caillard, J.-L. Martin, *Thermally Activated Mechanisms in Crystal Plasticity*, Pergamon, Boston, USA **2003**.

[57] N. Q. Chinh, T. Csanádi, T. Győri, R. Z. Valiev, B. B. Straumal, M. Kawasaki, T. G. Langdon, *Mater. Sci. Eng. A* **2012**, *543*, 117.

[58] A. Leitner, V. Maier-Kiener, J. Jeong, M. D. Abad, P. Hosemann, S. H. Oh, D. Kiener, *Acta Mater.* **2016**, *121*, 104.

[59] V. Maier, A. Leitner, R. Pippan, D. Kiener, *JOM* **2015**, *67*, 2934.

[60] V. Maier-Kiener, B. Schuh, E. P. George, H. Clemens, A. Hohenwarter, *Mater. Des.* **2017**, *115*, 479.

[61] V. Maier-Kiener, B. Schuh, E. P. George, H. Clemens, A. Hohenwarter, *J. Mater. Res.* **2017**, *32*, 2658.

[62] D.-H. Lee, I.-C. Choi, G. Yang, Z. Lu, M. Kawasaki, U. Ramamurty, R. Schwaiger, J.-i. Jang, *Scripta Mater.* **2018**, *156*, 129.

[63] D.-H. Lee, J.-M. Park, G. Yang, J. He, Z. Lu, J.-Y. Suh, M. Kawasaki, U. Ramamurty, J.-i. Jang, *Scripta Mater.* **2019**, *163*, 24.

[64] B. Ahn, H.-J. Lee, I.-C. Choi, M. Kawasaki, J.-i. Jang, T. G. Langdon, *Adv. Eng. Mater.* **2016**, *18*, 1001.

[65] V. Maier, A. Hohenwarter, R. Pippan, D. Kiener, *Scripta Mater.* **2015**, *106*, 42.

[66] I.-C. Choi, C. Brandl, R. Schwaiger, *Acta Mater.* **2017**, *140*, 107.

[67] D.-H. Lee, M.-Y. Seok, Y. Zhao, I.-C. Choi, J. He, Z. Lu, J.-Y. Suh, U. Ramamurty, M. Kawasaki, T. G. Langdon, J.-i. Jang, *Acta Mater.* **2016**, *109*, 314.

[68] H. Li, A. H. W. Ngan, *J. Mater. Res.* **2004**, *19*, 513.

[69] I.-C. Choi, B.-G. Yoo, Y.-J. Kim, M.-Y. Seok, Y. Wang, J.-I. Jang, *Scripta Mater.* **2011**, *65*, 300.

[70] H. Conrad, *Mater. Sci. Eng. A* **2003**, *341*, 216.

[71] A. S. Argon, *Strengthening Mechanisms in Crystal Plasticity*, Oxford University Press, Oxford **2008**.

[72] B. Schuh, F. M. Martin, B. Völker, E. P. George, H. Clemens, R. Pippan, A. Hohenwarter, *Acta Mater.* **2015**, *96*, 258.

[73] M. Vaidya, K. G. Pradeep, B. S. Murty, G. Wilde, S. V. Divinski, *Sci. Rep.* **2017**, *7*, 12293.

1900648 (10 of 10)